

Study of the $\gamma p \rightarrow \eta p$ reaction with the Crystal Ball detector at the Mainz Microtron (MAMI-C)

E. F. McNicoll¹, S. Prakhov^{2†}, I. I. Strakovsky^{3§}, P. Aguar-Bartolomé⁴, L. K. Akasoy⁴, J. R. M. Annand¹, H. J. Arends⁴, R. A. Arndt^{3*}, Ya. I. Azimov⁵, K. Bantawa⁶, R. Beck⁷, V. S. Bekrenev⁵, H. Berghäuser⁸, A. Braghieri⁹, D. Branford¹⁰, W. J. Briscoe³, J. Brudvik², S. Cherepnaya¹¹, R. F. B. Codling¹, B. T. Demissie³, E. J. Downie^{4,1,3}, P. Drexler⁸, L. V. Fil'kov¹¹, A. Fix¹², B. Freehart³, D. I. Glazier¹⁰, R. Gregor⁸, D. Hamilton¹, E. Heid^{4,3}, D. Hornidge¹³, I. Jaegle¹⁴, O. Jahn⁴, T. C. Jude¹⁰, V. L. Kashevarov¹¹, J. D. Kellie¹, I. Keshelashvili¹⁴, R. Kondratiev¹⁵, M. Korolija¹⁶, M. Kotulla⁸, A. A. Koulbardi⁵, S. P. Kruglov⁵, B. Krusche¹⁴, V. Lisin¹⁵, K. Livingston¹, I. J. D. MacGregor¹, Y. Maghrbi¹⁴, D. M. Manley⁶, Z. Marinides³, M. Martinez⁴, J. C. McGeorge¹, B. McKinnon¹, D. Mekterovic¹⁶, V. Metag⁸, S. Micanovic¹⁶, D. Middleton¹³, A. Mushkarenkov⁹, B. M. K. Nefkens², A. Nikolaev⁷, R. Novotny⁸, M. Ostrick⁴, P. B. Otte⁴, B. Oussena^{4,3}, M. W. Paris³, P. Pedroni⁹, F. Pheron¹⁴, A. Polonski¹⁵, J. Robinson¹, G. Rosner¹, T. Rostomyan^{9‡}, S. Schumann⁴, M. H. Sikora¹⁰, D. I. Sober¹⁷, A. Starostin², I. M. Suarez², I. Supek¹⁶, M. Thiel⁸, A. Thomas⁴, L. Tiator⁴, M. Unverzagt⁴, D. P. Watts¹⁰, D. Werthmüller¹⁴, R. L. Workman³, I. Zamboni¹⁶, and F. Zehr¹⁴

(Crystal Ball Collaboration at MAMI)

¹*Department of Physics and Astronomy, University of Glasgow, Glasgow G12 8QQ, United Kingdom*

²*University of California Los Angeles, Los Angeles, California 90095-1547, USA*

³*The George Washington University, Washington, DC 20052, USA*

⁴*Institut für Kernphysik, University of Mainz, D-55099 Mainz, Germany*

⁵*Petersburg Nuclear Physics Institute, 188300 Gatchina, Russia*

⁶*Kent State University, Kent, Ohio 44242, USA*

⁷*Helmholtz-Institut für Strahlen- und Kernphysik, University of Bonn, D-53115 Bonn, Germany*

⁸*II Physikalisches Institut, University of Giessen, D-35392 Giessen, Germany*

⁹*INFN Sezione di Pavia, I-27100 Pavia, Italy*

¹⁰*School of Physics, University of Edinburgh, Edinburgh EH9 3JZ, United Kingdom*

¹¹*Lebedev Physical Institute, 119991 Moscow, Russia*

¹²*Tomsk Polytechnic University, 634050 Tomsk, Russia*

¹³*Mount Allison University, Sackville, New Brunswick E4L3B5, Canada*

¹⁴*Institut für Physik, University of Basel, CH-4056 Basel, Switzerland*

¹⁵*Institute for Nuclear Research, 125047 Moscow, Russia*

¹⁶*Rudjer Boskovic Institute, HR-10000 Zagreb, Croatia and*

¹⁷*The Catholic University of America, Washington, DC 20064, USA*

(Dated: September 13, 2018)

The $\gamma p \rightarrow \eta p$ reaction has been measured with the Crystal Ball and TAPS multiphoton spectrometers in the energy range from the production threshold of 707 MeV to 1.4 GeV ($1.49 \leq W \leq 1.87$ GeV). Bremsstrahlung photons produced by the 1.5-GeV electron beam of the Mainz Microtron MAMI-C and momentum analyzed by the Glasgow Tagging Spectrometer were used for the η -meson production. Our accumulation of 3.8×10^6 $\gamma p \rightarrow \eta p \rightarrow 3\pi^0 p \rightarrow 6\gamma p$ events allows a detailed study of the reaction dynamics. The $\gamma p \rightarrow \eta p$ differential cross sections were determined for 120 energy bins and the full range of the production angles. Our data show a dip near $W = 1680$ MeV in the total cross section caused by a substantial dip in η production at forward angles. The data are compared to predictions of previous SAID and MAID partial-wave analyses and to the latest SAID and MAID fits that included our data.

PACS numbers: 11.80.Et,13.60.Le,25.20.Lj

I. INTRODUCTION

The N^* family of nucleon resonances has many well established members [1], several of which exhibit overlapping pole positions, very similar masses and widths, but different J^P spin-parity values. Apart

[†]Electronic address: prakhov@ucla.edu

[§]Electronic address: igor@gwu.edu

*Deceased

[‡]Present address: University of Basel, Switzerland

from the $N(1535)1/2^-$ state, the known photo-decay amplitudes have been determined from analyses of single-pion photoproduction, so the ηN branching ratios are in general poorly known. Evidently η -photoproduction data are required, and this work studies the region from threshold, where there are two closely spaced states: $N(1520)3/2^-$ and $N(1535)1/2^-$, up to center-of-mass (c.m.) energies of $W \approx 1800$ MeV, encompassing a sequence of six overlapping states: $N(1650)1/2^-$, $N(1675)5/2^-$, $N(1680)5/2^+$, $N(1700)3/2^-$, $N(1710)1/2^+$, and $N(1720)3/2^+$. Compared to pion photoproduction, the η channel has some advantages. Isospin conservation requires that η production probes only $I = 1/2$ contributions, simplifying the extraction of individual N^* properties. Couplings of N^* s to the ηN channel, in comparison with the πN couplings, may clarify the inner structure of resonances.

New, high quality data on $\gamma p \rightarrow \eta p$ are needed to shed light on these issues, and the tagged-photon hall at Mainz offers a state-of-the-art facility to obtain such data. Here we report on a new differential-cross-section measurement, covering incident photon energies from threshold ($E_\gamma = 707$ MeV) up to $E_\gamma = 1400$ MeV. The accumulation of 3.8×10^6 events for the process $\gamma p \rightarrow \eta p \rightarrow 3\pi^0 p \rightarrow 6\gamma p$ has enabled the data to be binned finely in E_γ (bin widths as small as ~ 4 MeV) and in η production angle, which in the c.m. frame is fully covered. The present measurement is part of an extensive program at the Mainz Microtron to provide data of unrivaled quality on neutral meson photoproduction, which includes polarized beam and target observables in addition to cross sections.

Our energy range includes several well-established resonances and also some more questionable ones. Indeed, the excellent photon-energy resolution offers the potential to illuminate any narrow states, possibly of exotic structure. Most of the states presently covered appear to have very small coupling to the ηN channel, and this in itself can be puzzling. For example, it is unclear why the ηN branching ratio is so small for the second S_{11} , $N(1650)1/2^-$, compared to the first $N(1535)1/2^-$. The data available for $\pi^- p \rightarrow \eta n$ are inadequate to study this question [2, 3]. The reason for a small branching ratio of $N(1520)3/2^-$ to ηN [1, 4] has to be understood, too. The Particle-Data-Group (PDG) estimate for the $A_{3/2}$ decay amplitude of the $N(1720)3/2^+$ state is consistent with zero, while the recent SAID determination gives a small but non-vanishing value [5]. The reason for the disagreement between the PDG estimate for the $A_{1/2}$ decay amplitude and the recent SAID determination [5] is also unclear. Other unresolved issues relate to the second P_{11} and D_{13} resonances [$N(1710)1/2^+$ and $N(1700)3/2^-$] that are not seen in the recent πN partial-wave analysis (PWA) [2], contrary to other PWAs used

by the Particle Data Group [1]. The ηN decay channel could be more favorable than πN for these states. The present data should have sufficient precision to allow reliable extraction of the ηN partial waves for these resonances, which will enhance our understanding of their internal dynamics. In addition, since the present data have good coverage of the ηp -threshold region, the S-wave dominance of the threshold behavior can also be checked.

The paper is laid out in the following manner: the experimental setup is briefly described in Sec. II; the procedure to determine the differential cross sections is described in Sec. III; the estimation of our systematic uncertainties is given in Sec. IV; the experimental results are presented in Sec. V; analyses of the data in terms of SAID and MAID are described in Sec. VI; finally, the findings of our study are summarized in Sec. VII.

Since the present data on $\gamma p \rightarrow \eta p \rightarrow 3\pi^0 p$ were also used in the determination of the slope parameter α for the $\eta \rightarrow 3\pi^0$ decay [6], a more detailed description of the experiment and data handling can be found in Ref. [6].

II. EXPERIMENTAL SETUP

The process $\gamma p \rightarrow \eta p \rightarrow 3\pi^0 p \rightarrow 6\gamma p$ was measured using the Crystal Ball (CB) [7] as the central spectrometer and the Two-Arm Photon Spectrometer (TAPS) [8, 9] as a forward spectrometer. These detectors were installed in the tagged bremsstrahlung photon beam of the Mainz Microtron (MAMI) [10, 11], with the photon energies determined by the Glasgow Tagging Spectrometer [12–14].

The CB spectrometer is a sphere consisting of 672 optically insulated NaI(Tl) crystals, shaped as truncated triangular pyramids, which point toward the center of the sphere. Each NaI(Tl) crystal is 41 cm long, which corresponds to 15.7 radiation lengths. The crystals are arranged in two hemispheres that cover 93% of 4π sr, sitting outside a central spherical cavity with a radius of 25 cm, which is designed to hold the target and inner detectors. To allow passage of the beam, the regions of polar angle below 20° and above 160° are not populated. The energy resolution for electromagnetic showers in the CB can be described as $\Delta E/E = 0.020/(E[\text{GeV}])^{0.36}$. Shower directions are determined with a resolution in θ , the polar angle with respect to the beam axis, of $\sigma_\theta = 2^\circ\text{--}3^\circ$, under the assumption that the photons are produced in the center of the CB. The resolution in the azimuthal angle ϕ is $\sigma_\phi/\sin\theta$.

To cover the forward aperture of the CB, the TAPS calorimeter [8, 9] was installed 1.5 m downstream of the CB center. TAPS geometry is flexible and, for the present A2 experiment, it was configured as a “plug” for the forward-angle hole in CB acceptance. In this experiment,

TAPS was arranged in a plane consisting of 384 BaF₂ counters of hexagonal cross section, with an inner diameter of 5.9 cm and a length of 25 cm, which corresponds to 12 radiation lengths. One counter was removed from the center of the array, which has an over-all, hexagonal geometry in the x - y plane, to allow the passage of the photon beam. TAPS subtends the full azimuthal range for polar angles from 1° to 20°. The energy resolution for electromagnetic showers in the TAPS calorimeter can be described as $\Delta E/E = 0.018 + 0.008/(E[\text{GeV}])^{0.5}$. Because of the relatively long distance from the CB, the resolution of TAPS in the polar angle θ was better than 1°. The resolution of TAPS in the azimuthal angle ϕ is better than $1/R$ radian, where R is the distance in centimeters from the TAPS center to the point on the TAPS surface that corresponds to the θ angle.

The upgraded Mainz Microtron, MAMI-C, is a four stage accelerator, and its latest addition (the fourth stage) is a harmonic double-sided electron accelerator [11]. An electron-beam energy of 1508 MeV was used for the present experiment. Bremsstrahlung photons, produced by electrons in a 10- μm Cu radiator and collimated by a 4-mm-diameter Pb collimator, were incident on a 5-cm-long liquid hydrogen (LH₂) target located in the center of the CB. The energies of the incident photons were analyzed up to 1402 MeV by detecting the post-bremsstrahlung electrons in the Glasgow Tagger [12–14]. The Tagger is a broad-momentum-band, magnetic-dipole spectrometer that focuses post-bremsstrahlung electrons onto a focal-plane detector, consisting of 353 half-overlapping plastic scintillators. The energy resolution of the tagged photons is mostly defined by the overlap region of two adjacent scintillation counters (a tagger channel) and the electron beam energy. For a beam energy of 1508 MeV, a tagger channel has a width about 2 MeV at 1402 MeV and about 4 MeV at 707 MeV (the η -production threshold). Tagged photons are selected in the analysis by examining the correlation in time between a tagger channel and the experimental trigger derived from CB signals.

The LH₂ target is surrounded by a particle identification (PID) detector [15] which is a cylinder of length 50 cm and diameter 12 cm, built from 24 identical plastic scintillator segments, of thickness 0.4 cm. In conjunction with the CB, this identifies charged particles by the $\Delta E/E$ technique, although this facility was not used in the present analysis.

The experimental trigger had two main requirements. First, the sum of the pulse amplitudes from the CB crystals had to exceed a hardware threshold that corresponded to an energy deposit of ~ 320 MeV. Second, the number of “hardware” clusters in the CB had to be larger than 2. A “hardware” cluster is a group of 16 adjacent crystals in which at least one crystal has an energy

deposit larger than 30 MeV.

III. DATA HANDLING

The photoproduction of η was measured by using the $3\pi^0$ decay mode of this meson:

$$\gamma p \rightarrow \eta p \rightarrow 3\pi^0 p \rightarrow 6\gamma p. \quad (1)$$

The other main neutral decay mode, $\eta \rightarrow \gamma\gamma$, was not used in this measurement because a large number of $\eta \rightarrow \gamma\gamma$ events did not satisfy the experimental-trigger requirements. The acceptance determination for the two-photon final state then becomes highly sensitive to the trigger efficiency, calculated using a Monte Carlo (MC) simulation. On the contrary, the trigger efficiency for $\eta \rightarrow 3\pi^0$ events is close to 100%, so the systematic uncertainty in the acceptance caused by the trigger simulation is small. Additionally, the angular resolution for $\eta \rightarrow \gamma\gamma$ events is worse than for $\eta \rightarrow 3\pi^0$, and there is a substantial background from the $\gamma p \rightarrow \pi^0 p$ reaction, which requires a careful subtraction.

Process (1) was investigated by analysis of events having six and seven “software” clusters reconstructed in both the CB and TAPS. The six-cluster sample was used to search for the events in which only six photons were detected, while for seven clusters the recoiling proton was also detected.

The kinematic-fitting technique was used to test the reaction hypotheses needed in our analysis and to select good candidates for the events of interest. The details of our parametrization of the detector information and resolutions are given in Ref. [6]. The events that satisfied the hypothesis of reaction (1) at the 2% confidence level, CL, (i.e., with a probability of misinterpretation less than 2%) were accepted as $\eta \rightarrow 3\pi^0$ candidates. The kinematic-fit output was then used to reconstruct the kinematics of the reaction. Since each event in general included several tagger hits (due to the high rates in the tagger detector), the $\gamma p \rightarrow \eta p \rightarrow 3\pi^0 p \rightarrow 6\gamma p$ hypothesis was tested for each tagger hit. Selection was based on the hit time which was required to be within a selected window (detailed below) and the equivalent photon energy, which was required to be above the reaction threshold of 707 MeV. The tagger-hit time distribution for $\eta \rightarrow 3\pi^0$ event candidates is shown in Fig. 1(a). If an $\eta \rightarrow 3\pi^0$ event candidate from one trigger passed the 2% CL criterion for several tagger hits, they were analyzed as separate events. The width of the tagger-hit window was chosen to be substantially wider (80 ns for this analysis) than the peak caused by prompt coincidences between the tagger and trigger. The width of the prompt window, denoted by vertical lines in Fig. 1(a), was taken to be 10 ns in order to include all prompt events. Using a wider window for the random

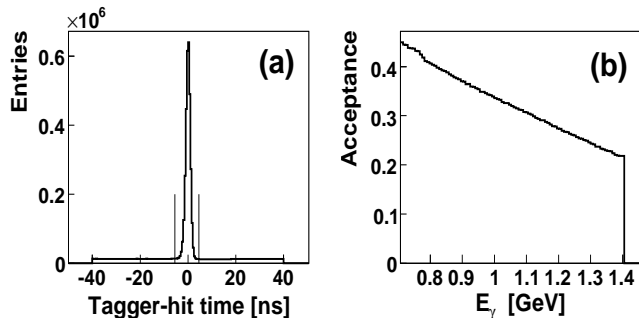


FIG. 1: (a) Tagger-hit time distribution for the experimental $\gamma p \rightarrow \eta p \rightarrow 3\pi^0 p$ events, where the two vertical lines define the region of prompt coincidences. (b) Detector acceptance for $\gamma p \rightarrow \eta p \rightarrow 3\pi^0 p$ events as a function of the incident-photon energy, E_γ .

coincidences allowed the collection of a sufficient number of events to determine precisely the random-background distribution beneath the prompt peak. The experimental distributions analyzed with the pure random events were then used to subtract the random background from the prompt-plus-random event sample. For our experimental conditions and for the chosen tagger-hit window, 40% of all event candidates were selected for more than one tagger hit. Since, for an event, there can be only one prompt tagger hit with the proper E_γ , there is no double counting of good events in the distributions with prompt candidates.

The Monte Carlo simulation of the $\gamma p \rightarrow \eta p \rightarrow 3\pi^0 p$ reaction that was used for the determination of the differential cross sections assumed an isotropic distribution of the production angle and independence of the reaction yield on the incident-photon energy. The simulation of the $\eta \rightarrow 3\pi^0$ decay was made according to phase space. The small deviation of the actual $\eta \rightarrow 3\pi^0$ decays from phase space was not significant in our analysis. All MC events were propagated through a GEANT (version 3.21) simulation of the CB-TAPS detector, folded with resolutions of the detectors and conditions of the trigger. The resultant simulated data were analyzed in the same way as the experimental data. The resulting detector acceptance for the $\gamma p \rightarrow \eta p \rightarrow 3\pi^0 p$ events selected by the kinematic fit at the 2% CL is shown in Fig. 1(b) as a function of the incident-photon energy, E_γ . It varies from about 45% at the η threshold to about 25% at an E_γ of 1.4 GeV. The agreement between the various experimental spectra and the spectra from the MC simulation has been illustrated in Ref. [6].

Besides the random-coincidence background, there are

two more background sources. The first one comes from interactions of incident photons with the target walls, which was investigated by analyzing the data taken when the target was empty. It was determined that the fraction of the empty-target background that remained in our $\eta \rightarrow 3\pi^0$ event candidates after applying the 2%-CL cut varied from 1% at reaction threshold to 2.7% at a beam energy of 1.4 GeV. The background spectra determined from the analysis of the empty-target samples were then subtracted from our full-target spectra.

Another source of background is the set of $\gamma p \rightarrow 3\pi^0 p$ events that are not produced by $\eta \rightarrow 3\pi^0$ decays. When the invariant mass of the three neutral pions in the final state is sufficiently close to the mass of the η meson, those events are selected as $\eta \rightarrow 3\pi^0$ candidates. A phase-space simulation of $\gamma p \rightarrow 3\pi^0 p$ was used for the subtraction of this background. The fraction of this direct $3\pi^0$ background in our $\eta \rightarrow 3\pi^0$ candidates was determined in each photon-energy bin via the normalization of the MC simulation for $\gamma p \rightarrow 3\pi^0 p$ to the corresponding experimental spectra (Fig. 2). The $3\pi^0$ invariant-mass distributions obtained from kinematic fitting to the $\gamma p \rightarrow 3\pi^0 p$ hypothesis were used for this purpose. In Fig. 2, these distributions are shown for the experimental data and MC simulation at incident-photon energies between 1150 MeV and 1200 MeV. The experimental spectrum after the subtraction of random-coincidence and empty-target backgrounds is shown in Fig. 2(a). The experimental events that were then selected as $\eta \rightarrow 3\pi^0$ candidates are shown in Fig. 2(b). The corresponding spectra obtained for the MC simulation of $\gamma p \rightarrow 3\pi^0 p$ are shown in Figs. 2(c) and (d). The MC-simulation spectrum in Fig. 2(c) has a shape very similar to that of the experimental spectrum under the η peak in Fig. 2(a), and its normalization to the data provides a good estimate of the direct $3\pi^0$ background in the $\eta \rightarrow 3\pi^0$ candidates. The fraction of direct $3\pi^0$ background that was subtracted from our experimental spectra was found to vary from 0.3% at the η threshold to 4.4% at 1.4 GeV.

The large number of events accumulated allowed the division of the data into 120 bins in E_γ . From the reaction threshold to an E_γ of 1008 MeV, the bin width was that of a single tagger channel (~ 4 MeV). From 1008 to 1238 MeV, two tagger channels were combined to a single energy bin. Above 1238 MeV, an energy bin included from three to eight tagger channels. The $\gamma p \rightarrow \eta p$ differential cross sections were determined as a function of $\cos\theta$, where θ is the polar angle of the η direction in the c.m. frame. The $\cos\theta$ spectra at all energies were divided into 20 bins.

The determination of the differential cross sections is illustrated in Figs. 3 and 4 for incident-photon energies of 760 and 1060 MeV, respectively. The experimental dis-

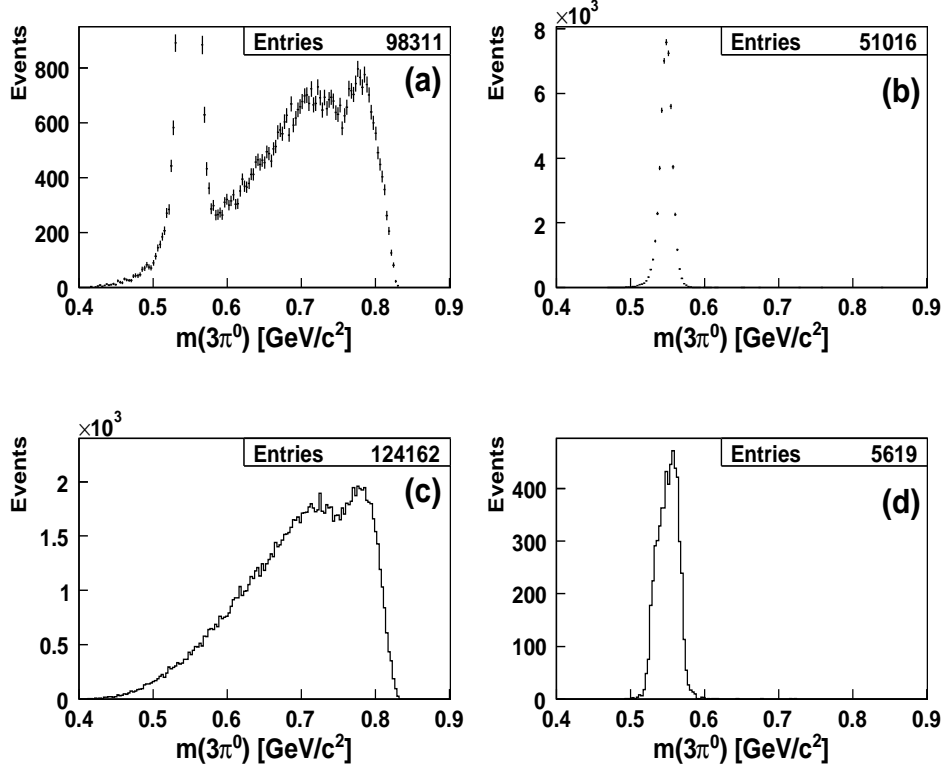


FIG. 2: Spectra of the $3\pi^0$ invariant mass obtained from kinematic fitting to the $\gamma p \rightarrow 3\pi^0 p$ hypothesis for the events with values of E_γ between 1150 and 1200 MeV: (a) experimental spectrum after the subtraction of the random and empty-target backgrounds, (b) experimental events selected also as $\eta \rightarrow 3\pi^0$ candidates, (c) MC simulation for $\gamma p \rightarrow 3\pi^0 p$, (d) events from the MC simulation for $\gamma p \rightarrow 3\pi^0 p$ selected also as $\eta \rightarrow 3\pi^0$ candidates.

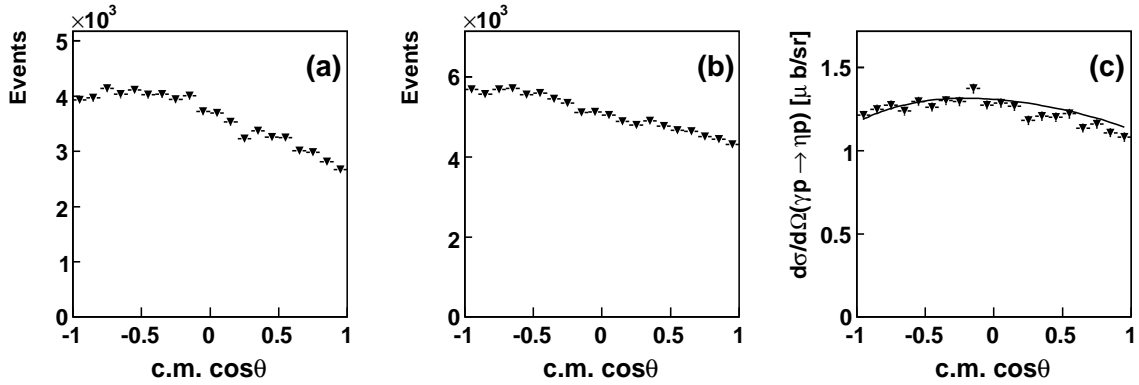


FIG. 3: $\cos\theta$ distributions in the c.m. frame of η photoproduction at $E_\gamma = 760$ MeV ($W = 1519$ MeV): (a) experimental $\gamma p \rightarrow \eta p \rightarrow 3\pi^0 p$ events; (b) MC simulation for the $\gamma p \rightarrow \eta p \rightarrow 3\pi^0 p$ events; (c) results for the $\gamma p \rightarrow \eta p$ differential cross section compared to the prediction by SAID (solution E429) [16] (solid line).

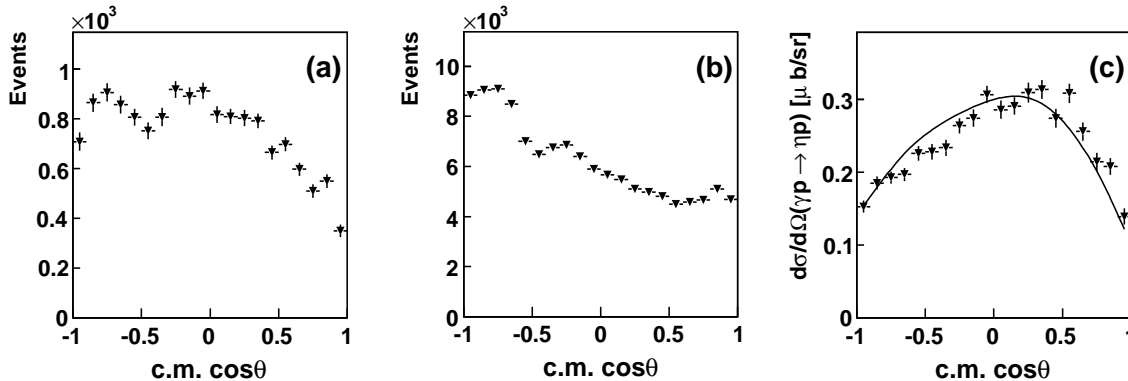


FIG. 4: Same as Fig. 3 but for $E_\gamma = 1060$ MeV ($W = 1694$ MeV).

tributions after subtraction of all background contributions are shown in Figs. 3(a) and 4(a). The corresponding distributions from the MC simulation are shown in Figs. 3(b) and 4(b). Since the simulated angular distribution is isotropic, the MC spectra reflect the experimental acceptance as a function of $\cos\theta$. The change in the acceptance with the incident-photon energy is caused by a more pronounced Lorentz boosting to forward angles, so that a larger fraction of particles impinge upon the overlap region between the CB and TAPS, where the metal framework of the CB aperture reduces detection efficiency. To obtain the $\gamma p \rightarrow \eta p$ differential cross sections, the experimental distributions were normalized for the acceptance, the $\eta \rightarrow 3\pi^0$ branching ratio, the photon beam flux, and the number of target protons. These differential cross sections are shown in Figs. 3(c) and 4(c). The results are very close to the predictions of SAID [16] for the $\gamma p \rightarrow \eta p$ differential cross sections at the given energies. These predictions are shown by the solid lines in the same figures.

IV. SYSTEMATIC UNCERTAINTIES

The results presented for the total, $\sigma_t(\gamma p \rightarrow \eta p)$, and differential cross sections include only statistical uncertainties. The largest contributions to the systematic uncertainty come from the calculation of the experimental acceptance by the MC simulation and from the determination of the photon-beam flux. A good test of the MC simulation is the determination of the $\gamma p \rightarrow \eta p$ differential cross sections using the two different modes of η decays: $\eta \rightarrow 3\pi^0$ and $\eta \rightarrow \gamma\gamma$. As discussed above, the data used in the present analysis were taken with the trigger suppressing the events with low cluster multiplicity in the final state. To perform our test, we used a data sample that contained much fewer events, taken at a later

stage with an almost open trigger. The results obtained for the $\gamma p \rightarrow \eta p$ total cross sections from the two different decay modes of η are in good agreement within their statistical uncertainties, the magnitude of which are $\sim 2\%$ for $\eta \rightarrow 3\pi^0$ and $\sim 1\%$ for $\eta \rightarrow \gamma\gamma$. They also agree with the high-precision $\gamma p \rightarrow \eta p$ results presented here. Based on the comparison of our own results with each other and with the existing data in the region of the $N(1535)1/2^-$ (the most well-known region), the general systematic uncertainty in our $\gamma p \rightarrow \eta p$ cross sections was estimated to be 4%. To take into account the statistical uncertainties in the estimation of the tagging efficiency of every individual tagger channel, used for the photon-flux calculation, those uncertainties were added in quadrature with our general systematic uncertainty. The typical magnitudes of the statistical uncertainties in the tagging efficiencies of the tagger channels for our data are between 1.4% at the η threshold and 2.5% at the largest energies. For every post-bremsstrahlung electron detected by a tagger channel, the tagging efficiency reflects a probability of the corresponding bremsstrahlung photon to pass through the photon collimator and to reach the target. The typical tagging efficiency of the tagger channels in the present experiment varied between 67% – 71%.

V. RESULTS

Since our results for the $\gamma p \rightarrow \eta p$ differential cross sections consist of 2400 experimental points, they are not tabulated in this publication, but are available in the SAID database [16] along with their uncertainties and the energy binning. In this section, we compare our results to the world data set.

In Fig. 5, our differential cross sections for four incident-photon energies are compared to previous measurements made at similar energies [17–23]. Some of

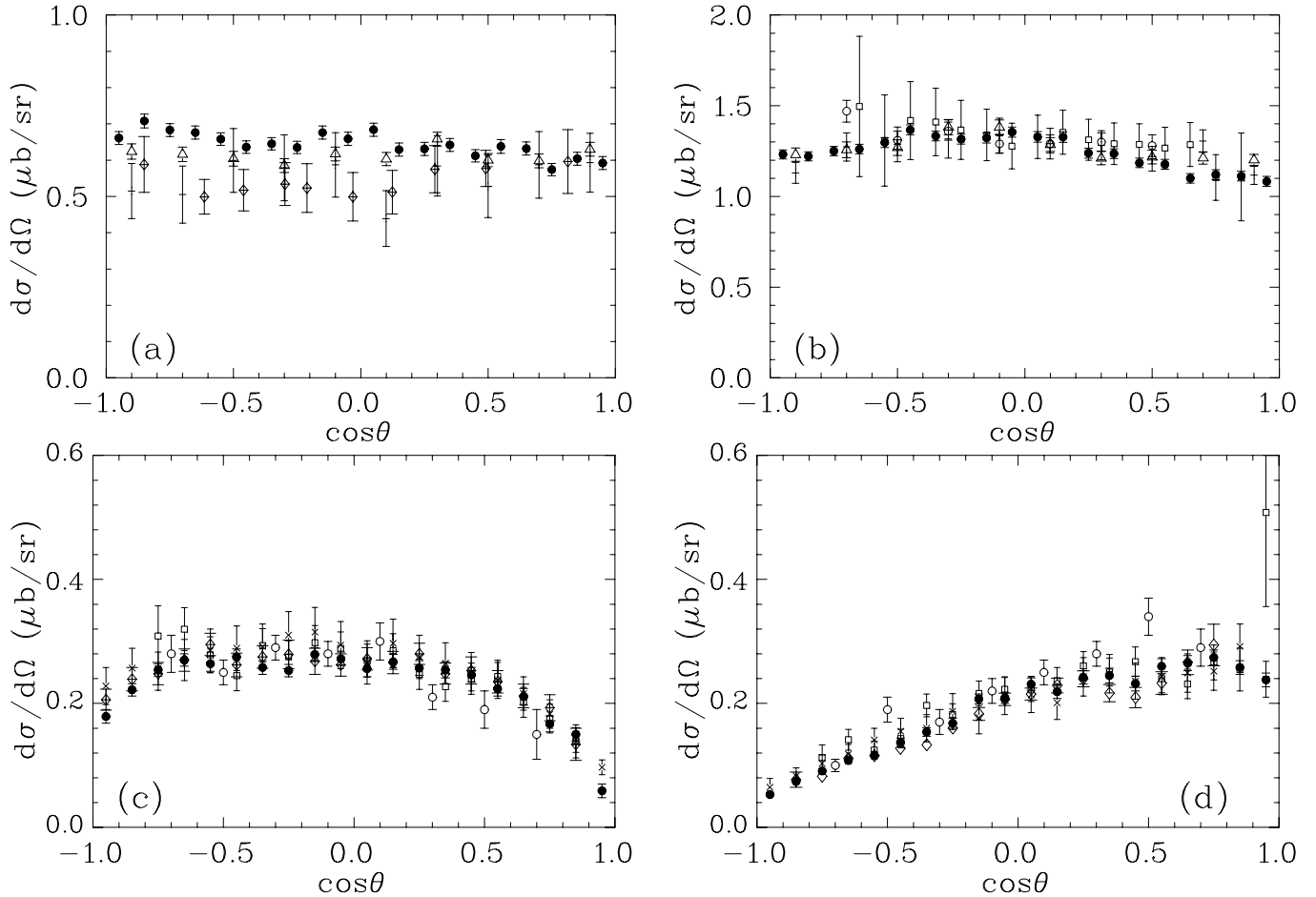


FIG. 5: Differential cross sections for $\gamma p \rightarrow \eta p$ as a function of $\cos \theta$, where θ is the production angle of η in the c.m. frame. The present data (solid circles) are shown for four energy bins: (a) $E_\gamma = 714.5 \pm 2.1$ MeV, (b) 772.9 ± 2.1 MeV, (c) 1026.8 ± 3.7 MeV, and (d) 1376.2 ± 9.7 MeV. Previous data are shown for experiments at MAMI-B [17] for 715.9 ± 5 MeV and 775.3 ± 5 MeV (open triangles); CLAS-g1c [18] for 775 ± 25 MeV, 1025 ± 25 MeV, and 1375 ± 25 MeV (open circles); CLAS-g11a [19] for 1384 ± 10 MeV (open diamonds); GRAAL [20] for 714 ± 9 MeV and 1024 ± 9 MeV (open diamonds with crosses); LNS [21] for 718.0 ± 10 MeV and 768.8 ± 10 MeV (horizontal bars); CB-ELSA [22] for 774 ± 25 MeV, 1025 ± 25 MeV, and 1374 ± 25 MeV (open squares); and CB-ELSA/TAPS [23] for 1025 ± 25 MeV and 1375 ± 25 MeV (crosses). Plotted uncertainties are statistical only.

these measurements [19, 23, 24] are quite recent, demonstrating the general desire of the resonance-physics community to obtain new $\gamma N \rightarrow \eta N$ data, which are needed for a better determination of the properties of the N^* states. The lowest energy shown, $E_\gamma = 714.5$ MeV ($W = 1490.3$ MeV), is close to the η -production threshold. The second energy, $E_\gamma = 772.9$ MeV ($W = 1526.7$ MeV), is at the maximum of the total cross section. The third energy, $E_\gamma = 1026.8$ MeV ($W = 1675.4$ MeV), is at a local minimum of the total cross section. The last energy shown, $E_\gamma = 1376.2$ MeV ($W = 1860.9$ MeV) is close to the maximum of our incident-photon energy range. As seen in Fig. 5, all our results are in reasonable agreement with the previous measurements, but our statistical uncertain-

ties are much smaller and the energy binning much finer. Larger discrepancies are observed between the data obtained close to the η -production threshold, but this can be explained by the difference in the energy binning of the data sets, bearing in mind the rapidly rising cross section close to threshold.

The present total cross sections for $\gamma p \rightarrow \eta p$ are obtained by integration of the differential cross sections. In Fig. 6, our total cross sections are compared with previous measurements [17–23] over the full energy range presently measured. A part of this distribution is repeated in Fig. 7(a), showing the range from the threshold to the $N(1535)1/2^-$ maximum in more detail. Our results for the total cross sections are in general agreement

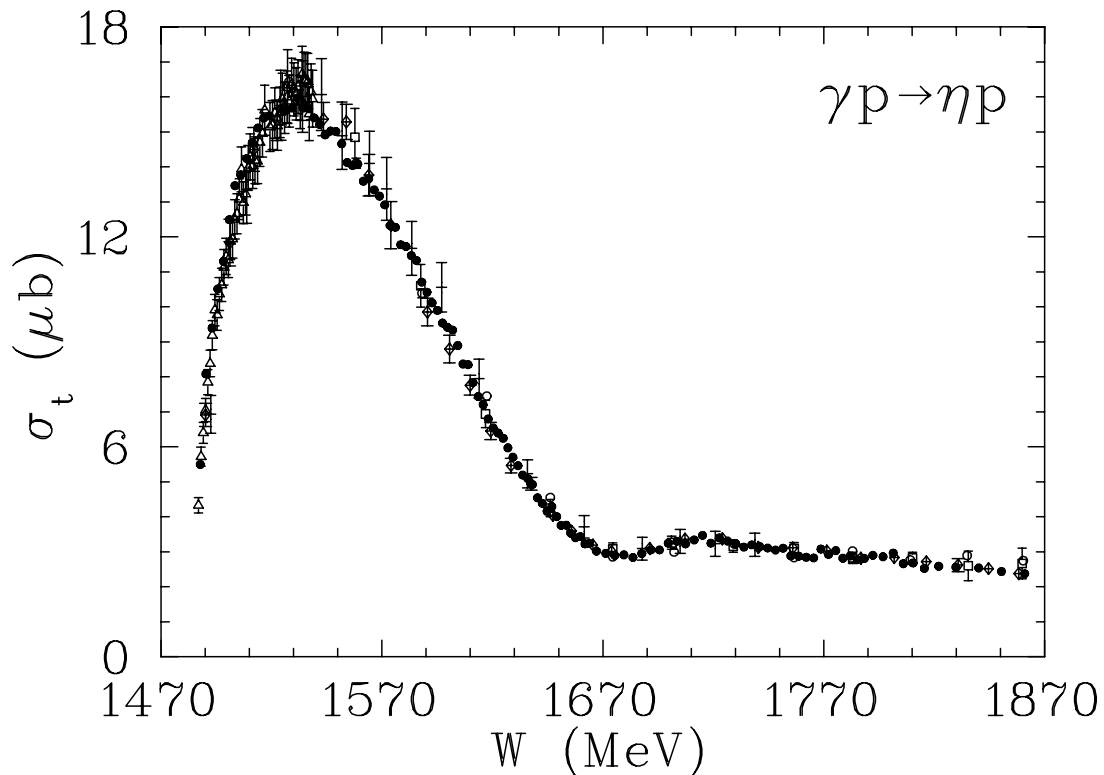


FIG. 6: Total cross section for $\gamma p \rightarrow \eta p$ as a function of the c.m. energy. Uncertainties plotted for our data are statistical only. Notation of different data is the same as in Fig. 5.

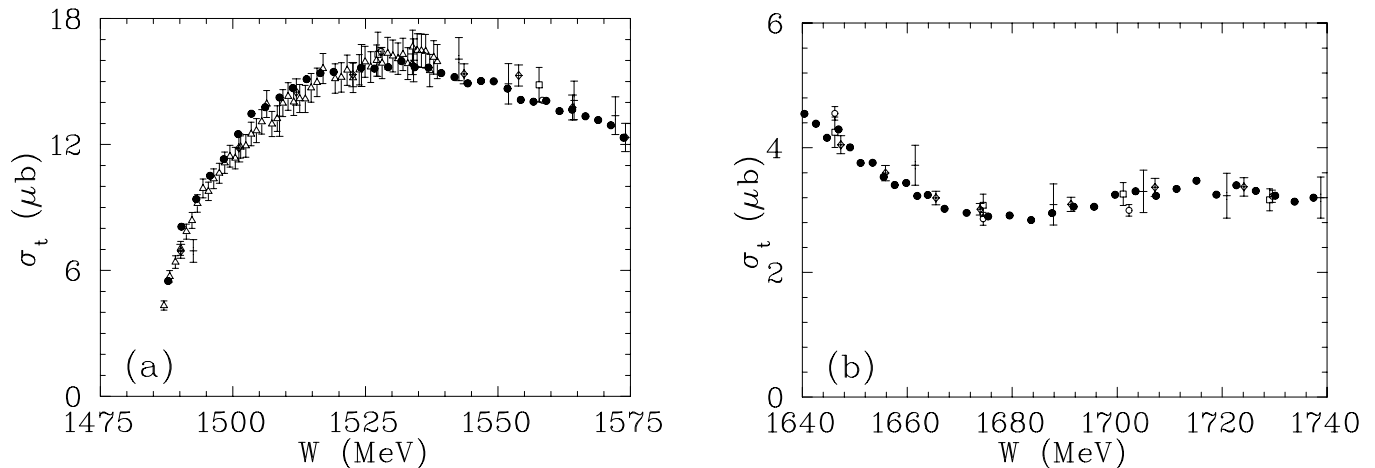


FIG. 7: Same as Fig. 6 but for narrower W ranges: (a) from the threshold to the maximum of the total cross section and (b) around a shallow dip, $W = 1680$ MeV.

with the major previous results. The energy range lying above a c.m. energy of 1640 MeV (see also Fig. 7(b)) is especially important for untangling the six overlapping N^* states and investigation of a possible narrow N^* state in the mass range ~ 1680 MeV. The $N^*(1680)$ was ex-

tracted in Ref. [25] from the πN PWA and suggested to be a member of the exotic anti-decuplet. Indeed a resonant bump at ~ 1680 MeV is observed in quasi-free $\gamma n \rightarrow \eta n$ [26–28]. However, for this reaction, the measured width of the bump was dominated by the experi-

mental energy resolution. Inspection of our $\sigma_t(\gamma p \rightarrow \eta p)$ energy dependence shows no evidence for a narrow bump related to a $N^*(1680)$ state in η photoproduction on a free proton. Rather our data show the existence of a shallow dip near $W = 1680$ MeV. However, such a situation may not contradict the existence of a narrow bump in η photoproduction on a neutron, since γn and γp couplings of the $N^*(1680)$ can be essentially different (as for an anti-decuplet member).

The full angular coverage of our differential cross sections allied with the small statistical uncertainties allows a reliable determination of the Legendre coefficients A_i , which was difficult to do with the previous data. This unprecedented detail of the energy dependence of the Legendre coefficients will be indispensable in untangling the properties of the N^* states lying in the present energy range. In Fig. 8, we illustrate Legendre coefficients $A_1 - A_3$ (higher orders are relatively insignificant) as a function of the c.m. energy. The swing in A_1 from negative to positive values in the vicinity of $W = 1680$ MeV is intriguing. Since the first coefficient, A_0 , simply reflects the magnitude of the total cross section, it is not shown.

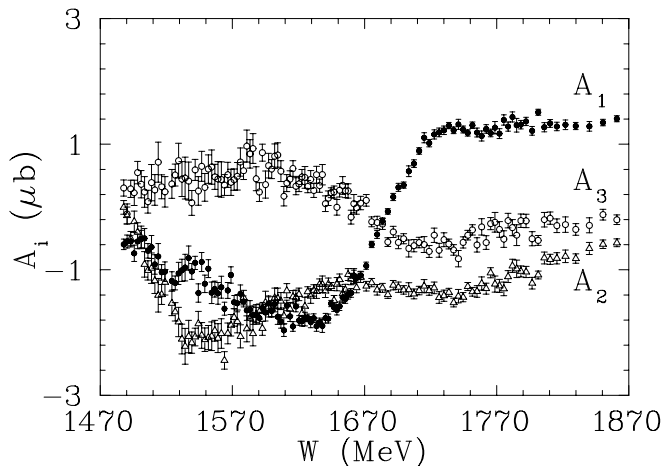


FIG. 8: Dominant Legendre coefficients from the fits to our differential cross sections. The coefficients are plotted as a function of the c.m. energy; A_1 is shown by solid circles, A_2 by open triangles, and A_3 by open circles.

VI. IMPACT OF THE DATA ON PWA

To gauge the influence of our data and their compatibility with previous measurements, our differential cross sections have been included in a number of fits using the full SAID database for $\gamma p \rightarrow \eta p$ up to $E_\gamma = 2.9$ GeV. The impact of our data on the SAID PWA can be understood from the comparison of the new

SAID fit GE09, which involves our data, with the previous SAID fit E429 [16]. The other data included in the GE09 fit involve all previously published data except recent CLAS-g11a [19], CB-ELSA/TAPS [23], and LEPS [24] differential cross sections. Our data were also included in the PWA under the Reggeized η -MAID model (Regge-MAID) [30] that was extended to a photon energy $E_\gamma = 3.7$ GeV ($W = 2.8$ GeV) by adding new resonances in the s -channel. Besides the resonances used in the original Regge-MAID [30], the new model includes five additional states from the fourth resonance group, namely $N(1900)3/2^+$, $N(2000)5/2^+$, $N(2080)3/2^-$, $N(2090)1/2^-$, and $N(2100)1/2^+$, which are needed to describe the latest data from CLAS-g11a [19] and CB-ELSA/TAPS [23]. The influence of these five states on the description of our data is very small. For the MAID solution without our data, we choose the η -MAID fit [29], in which E_γ is limited to 1.9 GeV ($W < 2.1$ GeV). The η -MAID analysis involves only the data published up to 2002. The details of the new SAID and Regge-MAID PWAs will be the subject of future publications.

To search for the minimum χ^2 value in the SAID fits, an overall rescaling of the differential cross sections was permitted within limits specified by the experimental systematic uncertainties [31]. A similar rescaling of the data, but without possible adjustment of the partial waves, was applied in the η -MAID and Regge-MAID fits. Comparison of the χ^2 values from the two SAID fits, E429 and GE09, and from the two MAID fits, η -MAID and new Regge-MAID, is given in Table I. The separate contri-

TABLE I: Comparison of the χ^2 values from the fits to the η -photoproduction data for the two SAID solutions, E429 and GE09, and the two MAID solutions, η -MAID and new Regge-MAID. The fits were performed for different E_γ ranges and amount of data in the databases used to fulfill the fits. See text for more details.

Solution	E_γ (MeV)	Data	χ^2/Data
GE09	< 2900	4211	1.5
E429	< 2900	1811	1.6
η -MAID	< 1900	1329	3.1
Regge-MAID	< 3700	4161	5.9

butions of individual data sets to the total χ^2 value are listed for each of the four $\gamma p \rightarrow \eta p$ analyses in Table II. These indicate that the more recent data sets display a greater degree of consistency. However, the description of the CLAS-g11a data is worse with the new fit GE09, compared to the previous solution E429. Although in the overlapping energy range $W = 1690$ to 1875 MeV, our data and the CLAS-g11a data are in good agreement.

In Fig. 9, we show our differential cross sections at 40

TABLE II: Individual contributions of different measurements of the differential cross sections to the total χ^2 value for the E429, GE09, η -MAID, and new Regge-MAID analyses of $\gamma p \rightarrow \eta p$ data. See text for details.

Experiment	E_γ (MeV)	W (MeV)	θ (deg)	Stat/Syst (%)	Data	χ^2/data		Ref
						E429–GE09– η -MAID–Regge-MAID		
CB-MAMI-C	707–1402	1487–1875	0–180	2/4	2400	5.5–1.4–6.8–3.2		This Work
GRAAL	714–1477	1491–1913	32–162	10/3	487	1.2–0.7–2.1–1.2		[20]
TAPS-MAMI-B	716–790	1493–1539	26–154	4/4	100	1.4–1.4–1.2–4.9		[17]
LNS	718–1142	1494–1740	26–154	2/6	180	0.9–1.5–0.9–2.3		[21]
CB-ELSA	774–2887	1530–2511	18–139	2/15	631	1.3–1.3–3.1–2.6		[22]
CLAS-g1c	775–1925	1530–2121	46–134	3/5	190	2.3–2.3–5.6–5.4		[18]
CB-ELSA/TAPS	875–2522	1590–2372	18–162	4/10	680	2.6–2.6–11.2–3.3		[23]
CLAS-g11a	1044–2861	1690–2502	33–148	7/11	979	4.3–5.7–12.0–9.5		[19]

energies and compare them with the results of each of the four PWA fits. In Fig. 10, a similar comparison is made for the excitation functions for eight production angles and for the full angular range. The number of the distributions shown is enough to illustrate the quality of our data, the main features of the $\gamma p \rightarrow \eta p$ dynamics at the measured energy range, and the impact of the present data on PWAs. The most noticeable effect of the present data on the new GE09 and Regge-MAID is due to very good measurements of the forward-angle cross sections for W in the range between 1545 and 1675 MeV. Earlier, this forward region either had been measured with worse accuracy or could only be reached by extrapolation.

For completeness, in Fig. 11 we compare the GE09, E429, η -MAID, and new Regge-MAID solutions for the $\gamma p \rightarrow \eta p$ excitation function at the extreme production angles: forward ($\theta = 0^\circ$) and backward ($\theta = 180^\circ$). The new data along with the new fits definitely indicate the existence of a dip structure around $W = 1670$ MeV, which has already been seen in our total cross section (see Fig. 6) and becomes very pronounced at forward production angles of η (see Figs. 10 and 11). This feature was missed or questionable in the analysis of the previous data.

Traditionally, to illustrate resonance masses and widths, the total cross section is plotted as a function of the c.m. energy. As seen in Figs. 6 and 7, the $\gamma p \rightarrow \eta p$ total cross section rises sharply above the reaction threshold. Such behavior is usually attributed to the dominance of the $N(1535)1/2^-$ resonance, having a mass close to the η production threshold ($W = 1487$ MeV) and a strong coupling to the ηN channel. Generally, the cross section for any process with a two-particle final state has the form $[(p^*/W) F(W)]$. The first factor comes from the phase-space integration, and p^* is the final-state relative momentum in the c.m. frame. The second factor $F(W)$ is determined by amplitudes. The essential point is that W and $F(W)$ depend explicitly only on

$(p^*)^2$, not on p^* . In terms of the final-state parameters, W depends on masses and $(p^*)^2$. Therefore, the near-threshold structure of the cross section should look as a series in the odd powers of p^* . Our data for $\gamma p \rightarrow \eta p$ are well described up to $p_\eta^* \sim 200$ MeV/c as $a_1 p_\eta^* + a_3 (p_\eta^*)^3$ with $a_1 = (6.79 \pm 0.09) \times 10^{-2} \mu b/(\text{MeV}/c)$ and $a_3 = -(7.24 \pm 0.22) \times 10^{-7} \mu b/(\text{MeV}/c)^3$ (see Fig. 12). Contributions to the cubic term come both from P-wave amplitudes and from W -dependence of the S-wave amplitude, which is essential due to the near-threshold dominance of the S-wave resonance $N(1535)1/2^-$. Note that the characteristic momentum for changes in our fit is $\sqrt{|a_1/a_3|} \sim 300$ MeV/c, while the maximum of the resonance peak corresponds to $p_\eta^* \sim 175$ MeV/c (see Fig. 12). The good quality of our data reveals itself in very small fluctuations of experimental points with respect to the fit. For comparison, a similar threshold behavior has been also observed in $\pi^- p \rightarrow \eta n$ [4], but the fluctuations there were larger due to lower precision of the data, and the coefficient a_3 could not be determined reliably. In addition, our fit gives implicit confirmation of small coupling of the ηN channel with the D -wave resonance $N(1520)3/2^-$, which could generate an essential term $(p_\eta^*)^5$.

Due to the dominance of the low-energy S -wave multipole, this contribution is nearly model-independent up to $W = 1650$ MeV. The modulus of the corresponding amplitude is plotted in Fig. 13 for both the SAID and MAID solutions. Phase differences are possible - these can be resolved in coupled-channel fits [32]. Figure 13 also shows the Breit-Wigner parameters, masses and widths, of two S_{11} resonances as found in the SAID PWA solution SP06 for the πN elastic scattering [2]. Note that $N(1650)1/2^-$ seems to be purely elastic, i.e., coupled only to the πN channel. If so, its contribution to η photoproduction should be small.

VII. SUMMARY AND CONCLUSIONS

The $\gamma p \rightarrow \eta p$ differential cross sections have been measured at the tagged photon facility of the Mainz Microtron MAMI-C using the Crystal Ball and TAPS spectrometers. The data span the photon-energy range 707 MeV to 1402 MeV and the full angular range in the c.m. frame. The accumulation of 3×10^6 $\gamma p \rightarrow \eta p \rightarrow 3\pi^0 p \rightarrow 6\gamma p$ events allows the fine binning of the data in energy and angle, which will enable the reaction dynamics to be studied in greater detail than previously possible. The present data agree well with previous equivalent measurements, but are markedly superior in terms of precision and energy resolution.

The present cross sections for the free proton show no evidence of enhancement in the region $W \sim 1680$ MeV, contrary to recent equivalent measurements on the quasi-free neutron [26–28]. However, this does not exclude the existence of an $N^*(1680)$ state as hypothesized in Ref. [25]. In the region around $W = 1680$ MeV, we rather observe a dip structure that becomes more pronounced at forward production angles of η . This feature was missed or questionable in the analysis of the previous data. The interpretation of this dip depends on dynamics.

Our $\gamma p \rightarrow \eta p$ data points have been included in a new SAID (GE09) and Regge-MAID PWAs, to which they made an substantial contribution, particularly for forward angles. Comparing to the previous SAID fit, E429, and to the η -MAID fit, the description of all existing

data by the new solutions, GE09 and Regge-MAID, is more satisfactory in the entire energy range.

We expect that the data presented in this paper will be invaluable for future partial-wave and coupled-channel analyses, in that they can provide much stronger constraints on the properties of the nucleon resonances from our energy region.

Acknowledgments

The authors thank the accelerator group of MAMI for their support. We thank the undergraduate students of Mount Allison University and The George Washington University for their assistance. This work was supported by the U.S. DOE (Grants No. DE-FG02-99ER41110 and DE-FG02-01ER41194), NSF (Grant No. PHY 0652549), the Jefferson Laboratory, the Southeastern Universities Research Association (DOE Contract No. DE-AC05-84ER40150), the U.K. Engineering and Physical Sciences Research Council, the U.K. Science and Technology Facilities Council, the Deutsche Forschungsgemeinschaft (SFB 443, SFB/TR 16), the European Community-Research Infrastructure Activity under the FP6 “Structuring the European Research Area” program (Hadron Physics, Contract No. RII3-CT-2004-506078), DFG-RFBR (Grant No. 09-02-91330) of Germany and Russia, SNF of Switzerland, NSERC of Canada, and Russian State Grant SS-3628.2008.2.

-
- [1] K. Nakamura *et al.* (Particle Data Group), *J. Phys. G* **37**, 075021 (2010).
 - [2] R. A. Arndt, W. J. Briscoe, I. I. Strakovsky, and R. L. Workman, *Phys. Rev. C* **74**, 045205 (2006).
 - [3] R. A. Arndt, W. J. Briscoe, M. W. Paris, I. I. Strakovsky, and R. L. Workman, *Chinese Phys. C* **33**, 1063 (2009). 045205 (2006).
 - [4] R. A. Arndt, W. J. Briscoe, T. W. Morrison, I. I. Strakovsky, R. L. Workman, and A. B. Gridnev, *Phys. Rev. C* **72**, 045202 (2005).
 - [5] M. Dugger *et al.* (CLAS Collaboration), *Phys. Rev. C* **79**, 065206 (2009).
 - [6] S. Prakhov *et al.*, *Phys. Rev. C* **79**, 035204 (2009).
 - [7] A. Starostin *et al.*, *Phys. Rev. C* **64**, 055205 (2001).
 - [8] R. Novotny, *IEEE Trans. Nucl. Sci.* **38**, 379 (1991).
 - [9] A. R. Gabler *et al.*, *Nucl. Instrum. Methods A* **346**, 168 (1994).
 - [10] H. Herminghaus *et al.*, *IEEE Trans. Nucl. Sci.* **30**, 3274 (1983).
 - [11] K.-H. Kaiser *et al.*, *Nucl. Instrum. Methods A* **593**, 159 (2008).
 - [12] I. Anthony *et al.*, *Nucl. Instrum. Methods A* **301**, 230 (1991).
 - [13] S. J. Hall *et al.*, *Nucl. Instrum. Methods A* **368**, 698 (1996).
 - [14] J. C. McGeorge *et al.*, *Eur. Phys. J. A* **37**, 129 (2008).
 - [15] D. Watts, *Proceedings of the 11th International Conference on Calorimetry in Particle Physics, Perugia, Italy, 2004* (World Scientific, 2005) p. 560.
 - [16] R. A. Arndt, W. J. Briscoe, M. W. Paris, I. I. Strakovsky, and R. L. Workman (unpublished). The full SAID database and numerous PWAs can be accessed at the website <http://gwdac.phys.gwu.edu>.
 - [17] B. Krusche *et al.*, *Phys. Rev. Lett.* **74**, 3736 (1995).
 - [18] M. Dugger *et al.* (CLAS Collaboration), *Phys. Rev. Lett.* **89**, 222002 (2002).
 - [19] M. Williams *et al.* (CLAS Collaboration), *Phys. Rev. C* **80**, 045213 (2009).
 - [20] O. Bartalini *et al.* (GRAAL Collaboration), *Eur. Phys. J. A* **33**, 169 (2007).
 - [21] T. Nakabayashi *et al.*, *Phys. Rev. C* **74**, 035202 (2006).
 - [22] V. Credé *et al.* (CB-ELSA Collaboration), *Phys. Rev. Lett.* **94**, 012004 (2005).
 - [23] V. Credé *et al.* (CB-ELSA/TAPS Collaboration), *Phys. Rev. C* **80**, 055202 (2009).
 - [24] M. Sumihama *et al.* (LEPS Collaboration), *Phys. Rev. C*

- 80**, 052201 (2009); private communications, 2009.
- [25] R. A. Arndt, Ya. I. Azimov, M. V. Polyakov, I. I. Strakovsky, and R. L. Workman, *Phys. Rev. C* **69**, 035208 (2004).
- [26] V. Kuznetsov *et al.* (by GRAAL Collaboration), *Phys. Lett. B* **647**, 23 (2007).
- [27] I. Jaegle *et al.* (CB-ELSA/TAPS Collaboration), *Phys. Rev. Lett.* **100**, 252002 (2008).
- [28] F. Miyahara *et al.*, *Prog. Theor. Phys. Suppl.* **168**, 90 (2007).
- [29] W.-T. Chiang, S.-N. Yang, L. Tiator, and D. Drechsel, *Nucl. Phys.* **A700**, 429 (2002).
- [30] W.-T. Chiang, S.-N. Yang, L. Tiator, M. Vanderhaeghen and D. Drechsel, *Phys. Rev. C* **68**, 045202 (2003).
- [31] R. A. Arndt, W. J. Briscoe, I. I. Strakovsky, and R. L. Workman, *Phys. Rev. C* **66**, 055213 (2002).
- [32] M. W. Paris and R. L. Workman, to be published in *Phys. Rev. C* (2010); arXiv:1004.0455 [nucl-th].

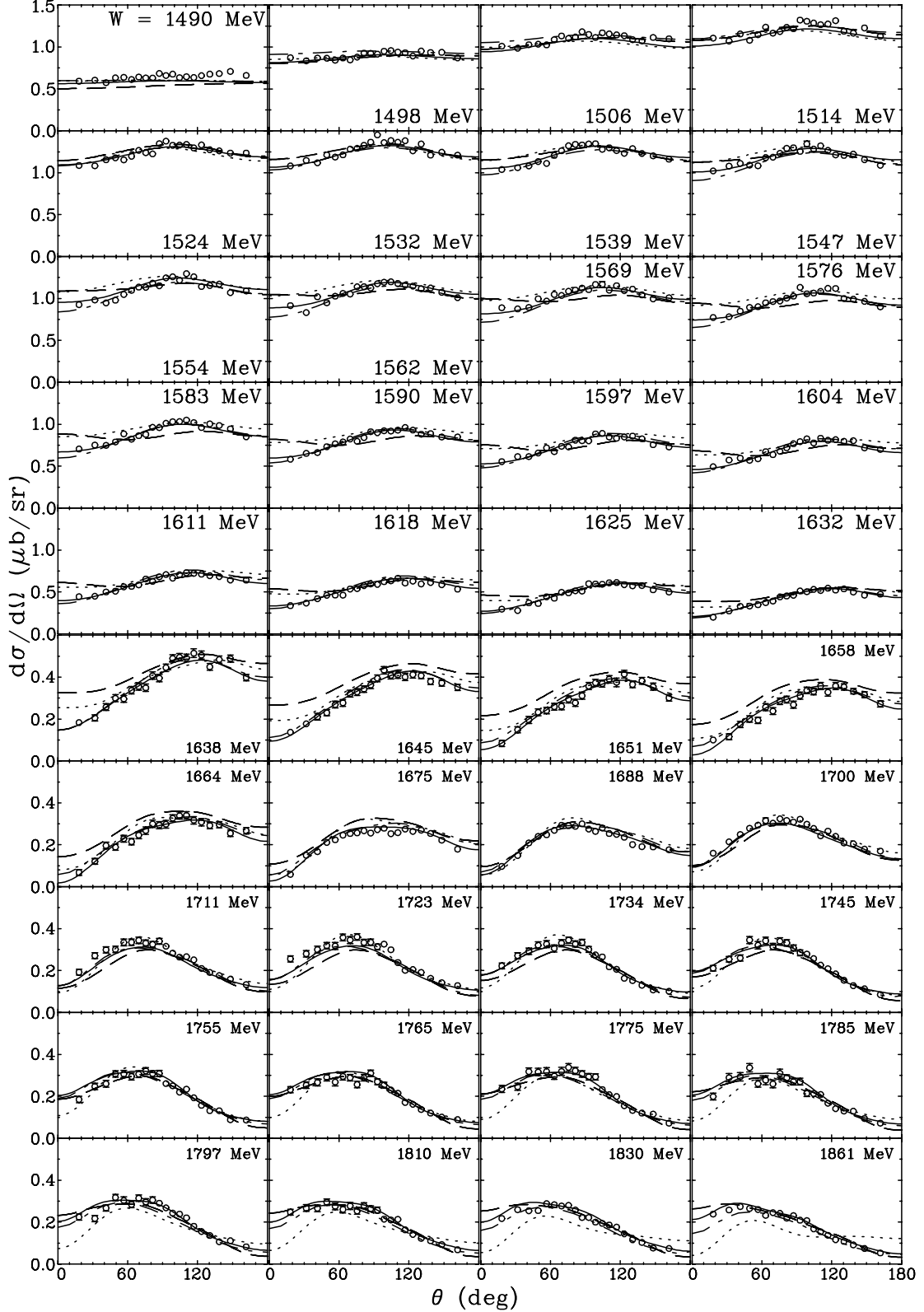


FIG. 9: Present differential cross sections (open circles) for $\gamma p \rightarrow \eta p$ as a function of θ , the η production angle in the c.m. frame, over the range of c.m. energies W presently measured. The plotted uncertainties are statistical only. The curves denote SAID solution GE09 (solid line), SAID solution E429 (dashed line), η -MAID solution (dotted line), and Regge-MAID solution (dot-dashed line).

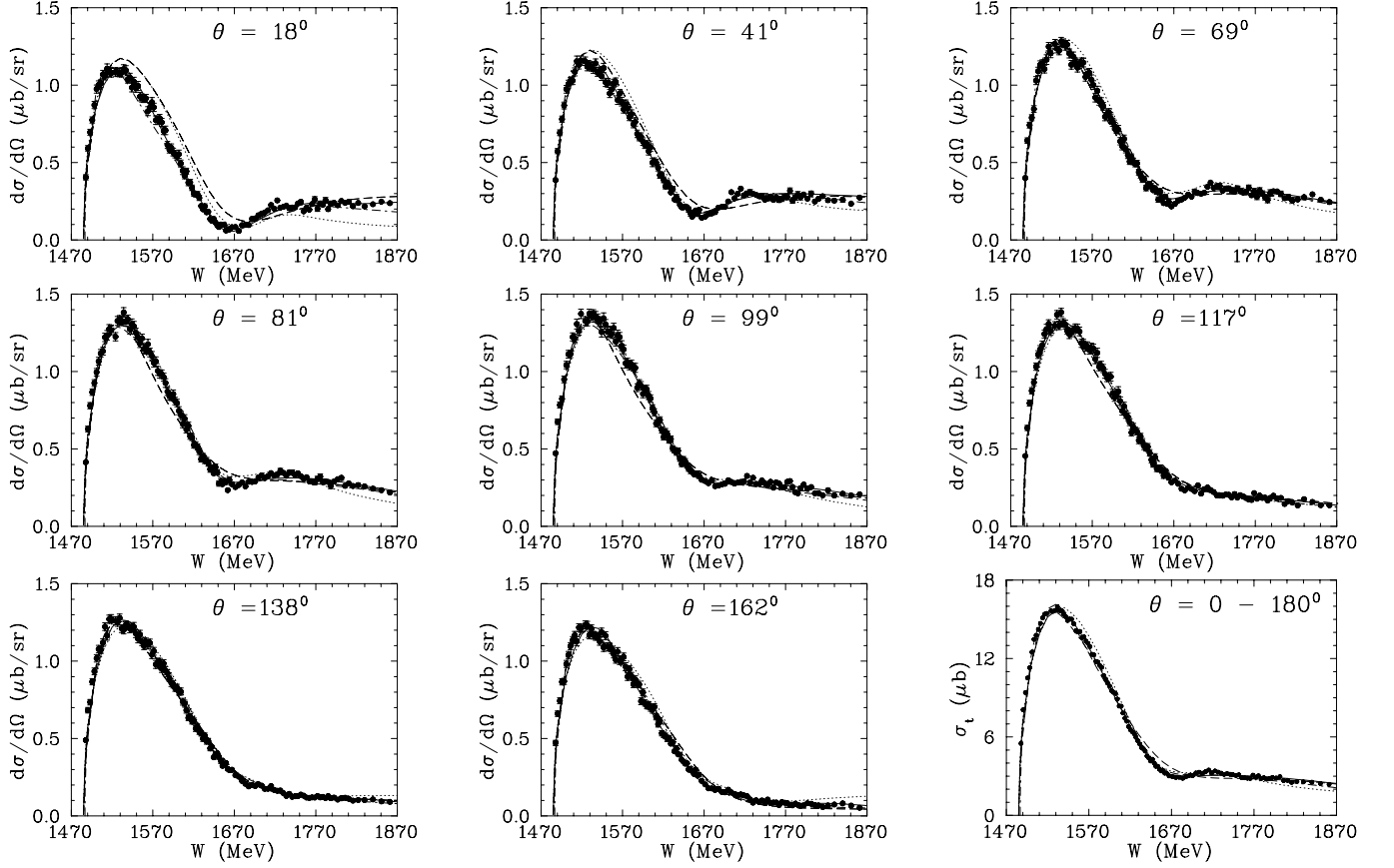


FIG. 10: Fixed-angle excitation functions for $\gamma p \rightarrow \eta p$ as a function of the c.m. energy W shown for eight values of the η production angle and for the full angular range. Our data are shown by solid circles. The plotted uncertainties are statistical only. The notation of the PWA solutions is the same as in Fig. 9.

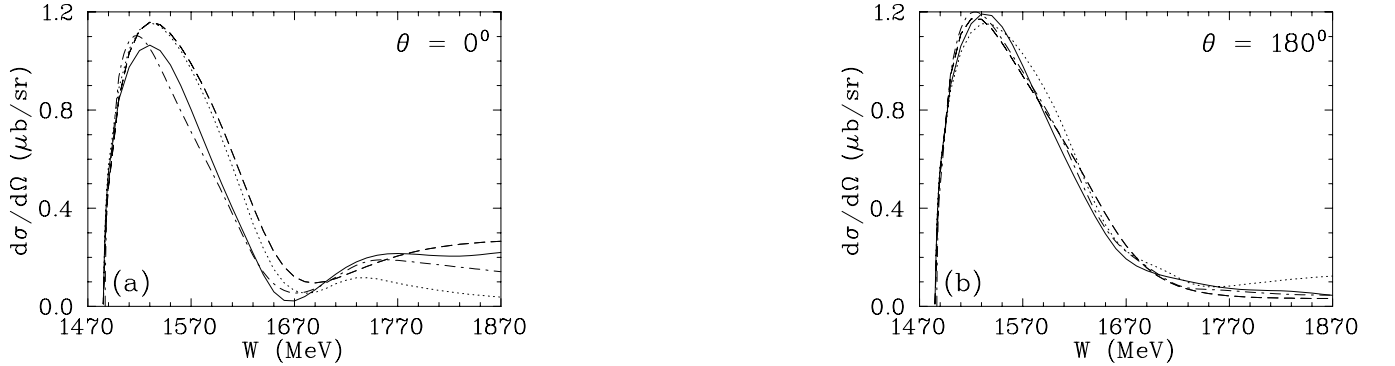


FIG. 11: PWA predictions for the $\gamma p \rightarrow \eta p$ excitation function at the extreme (forward and backward) production angles of η , shown as a function of the c.m. energy W . Notation of the PWA predictions is the same as in Fig. 9.

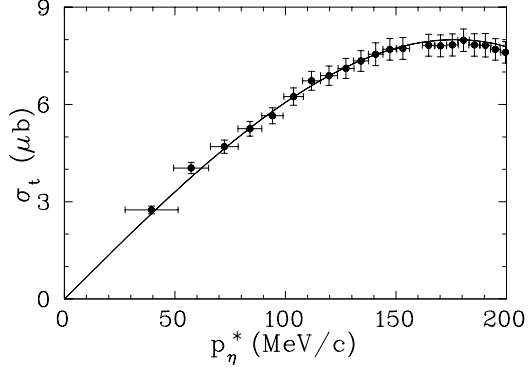


FIG. 12: Our total cross section (circles) for $\gamma p \rightarrow \eta p$ as a function of the η momentum in the c.m. frame. The solid line shows the results of fitting our data to a sum of linear and cubic terms.

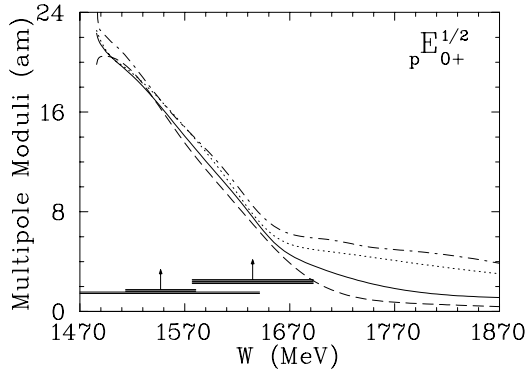


FIG. 13: Modulus of the multipole amplitude $S_{11pE} ({}_pE_{0+}^{1/2})$ for $\gamma p \rightarrow \eta p$ from the reaction threshold to $E_\gamma = 1.4$ GeV. Notations for the amplitude curves are the same as in Fig. 9. The vertical arrows indicate W_R (Breit-Wigner mass) and the horizontal bars show the full and partial width Γ for $\Gamma_{\pi N}$ associated with the SAID solution SP06 for πN [2].